

Herringbone structures during an X-class eruptive flare

QINGMIN ZHANG,¹ ZONGJUN NING,¹ XINGYAO CHEN,² WEI CHEN,¹ XIAOLI YAN,^{3,4} AND SHUYUE LI^{1,5}

¹*Purple Mountain Observatory, Chinese Academy of Sciences, Nanjing 210023, People's Republic of China*

²*State Key Laboratory of Solar Activity and Space Weather, National Space Science Center, Chinese Academy of Sciences, Beijing 100190, People's Republic of China*

³*Yunnan Observatories, Chinese Academy of Sciences, Kunming 650216, People's Republic of China*

⁴*Yunnan Key Laboratory of Solar Physics and Space Science, Kunming 650216, People's Republic of China*

⁵*School of Science, Nanjing University of Posts and Telecommunications, Nanjing 210023, People's Republic of China*

ABSTRACT

In this paper, we report quasi-periodic herringbone structures during the impulsive phase of an X-class flare, coinciding with the distinct acceleration phase of eruptive prominence ejection on 2023 December 31. The prominence propagates non-radially in the southeast direction with an inclination angle of $\sim 35^\circ$. The fast coronal mass ejection (CME) at a speed of $\sim 2852 \text{ km s}^{-1}$ drives a shock wave and a coronal EUV wave. The herringbone structures lasting for ~ 4 minutes take place at the initial stage of a group of type II radio burst. The herringbones in the frequency range 20–70 MHz are characterized by simultaneous forward-drift and reverse-drift bursts with average durations of $\sim 2.5 \text{ s}$ and $\sim 3.1 \text{ s}$. The frequency drift rates of these bursts fall in a range of $1.3\text{--}9.4 \text{ MHz s}^{-1}$ with average values of ~ 3.6 and $\sim 4.1 \text{ MHz s}^{-1}$, respectively. The speeds of electron beams producing the herringbones are estimated to be $0.04\text{--}0.41 c$, with average values of $\sim 0.23 c$ and $\sim 0.11 c$ for forward-drifting and reverse-drift bursts, respectively. The heights of particle acceleration regions are estimated to be $0.64\text{--}0.78 R_\odot$ above the photosphere, which are consistent with the height of CME front ($\sim 0.75 R_\odot$) when the shock forms. Quasi-periodic pulsations with periods of $17.5\text{--}21.3 \text{ s}$ are found in the radio fluxes of herringbones, suggesting that electrons are accelerated by the CME-driven shock intermittently.

Keywords: Sun prominences — Sun flares — Solar coronal mass ejections — Solar radio emission

1. INTRODUCTION

Solar flares and coronal mass ejections (CMEs) are the most spectacular eruptions as a result of impulsive energy releases in the solar system (L. Fletcher et al. 2011). Quasi-periodic pulsations (QPPs) could be observed in soft X-ray (SXR), hard X-ray (HXR), extreme ultraviolet (EUV), UV, and radio wavelengths (A. R. Inglis et al. 2008; X. Chen et al. 2019; I. V. Zimovets et al. 2021; S. Li et al. 2025). QPPs may reflect intermittent magnetic reconnections and particle accelerations in flares (Q. M. Zhang et al. 2016). Fast CMEs are likely to drive shock waves, which are usually associated with type II radio bursts in the metric and decameter wave ranges (G. Mann et al. 1995; B. Vršnak et al. 2002; P. Zucca et al. 2014). The frequencies of a type II burst drift slowly from high to low values as the CME propagates outward. Like termination shocks generated by reconnection outflow jets in solar flares (H. Aurass et al. 2002; B. Chen et al. 2015), CME-driven shocks are capable of accelerating particles to high energies as well (see G. P. Zank et al. 2007, and references therein). N. Gopalswamy et al. (2009b) investigated CMEs during the declining phase of solar cycle 23 and derived the CME heights when the related type II bursts start. The average distance is $\sim 1.5 R_\odot$, exactly consistent with the location at which the Alfvén speed reaches a minimum. Besides, the CME-driven shocks are most likely to accelerate electrons in the heliocentric distance of $1.5\text{--}4.0 R_\odot$. N. Gopalswamy et al. (2013) obtained the shock formation height ($\sim 1.38 R_\odot$) and the starting frequency ($\sim 85 \text{ MHz}$)

of a type II burst related with the CME on 2012 May 17. P. Zucca et al. (2014) reported that the shock forms at the CME flank with a height of $\sim 1.6 R_{\odot}$ on 2011 September 23.

Herringbones are fine structures related to type II radio bursts (J. A. Roberts 1959; I. H. Cairns & R. D. Robinson 1987; H. V. Cane & S. M. White 1989; G. Mann et al. 1995; G. Mann & A. Klassen 2005; V. V. Dorovskyy et al. 2015; A. Koval et al. 2023; D. E. Morosan et al. 2024). They are composed of simultaneous forward-drift and reverse-drift radio bursts in most cases (G. Mann et al. 1992). Sometimes, herringbones show merely forward-drift or reverse-drift bursts (I. H. Cairns & R. D. Robinson 1987; G. Mann & H. T. Classen 1995; J. Magdalenić et al. 2020). The drift rates of herringbones are a few MHz s^{-1} , which are much faster than typical type II bursts ($\sim 0.1 \text{ MHz s}^{-1}$). In a statistical study, G. Mann & A. Klassen (2002) found that the drift rates of herringbones are nearly half of those of type III bursts. Surprisingly, J. Magdalenić et al. (2020) reported a drift rate up to $\sim 25 \text{ MHz s}^{-1}$ of the herringbones on 2014 August 25. The durations of herringbones are mostly a few minutes (G. Mann et al. 1992; E. P. Carley et al. 2013, 2015; D. E. Morosan et al. 2019; E. P. Carley et al. 2021) and rarely up to ~ 20 minutes (D. E. Morosan et al. 2022). It is generally believed that herringbones are produced by high-energy electron beams repetitively accelerated by quasi-perpendicular CME-driven shocks, with the shock normal angle (θ_{BN}) between the shock normal and the upstream magnetic field being close to 90° (S. D. Bale et al. 1999). Specifically, these electrons are accelerated via shock drift acceleration at the wavy or rippled shock fronts so that electrons could be trapped and accelerated repeatedly to obtain very high energies (G. D. Holman & M. E. Pesses 1983; P. Zlobec et al. 1993; L. Ball & D. B. Melrose 2001; G. Mann & A. Klassen 2005; D. Burgess 2006; R. Miteva & G. Mann 2007; F. Guo & J. Giacalone 2010; M. Vandas & M. Karlický 2011; D. E. Morosan et al. 2024). The emission mechanism of herringbones is plasma emission (G. A. Dulk 1985). Consequently, propagations of these electrons toward and away from the Sun generate reverse-drift and forward-drift bursts, respectively. It is demonstrated that forward-drift herringbone shows an opposite sense of circular polarization to the reverse-drift herringbone (D. E. Morosan et al. 2022). Analysis of herringbone structures provides an efficient and useful tool to probe plasma turbulence in the corona (E. P. Carley et al. 2021; A. Koval et al. 2023).

Till now, herringbones have rarely been detected. It is found that only $\sim 20\%$ of type II bursts are associated with herringbones (I. H. Cairns & R. D. Robinson 1987; J. Magdalenić et al. 2020; E. P. Carley et al. 2021; D. E. Morosan et al. 2022, 2024). On 2011 September 22, a hot channel eruption occurred in NOAA active region (AR) 11302, producing an X1.4 class flare and a fast CME at a speed of $\sim 1905 \text{ km s}^{-1}$ (P. Zucca et al. 2014; Q. Zhang et al. 2023). A coronal shock and an extreme ultraviolet (EUV) wave are driven by the CME, which is associated with herringbone structures (E. P. Carley et al. 2013) detected by spectrometers at the e-Callisto⁶ (A. O. Benz et al. 2009) Rosse Solar Terrestrial Observatory (RSTO; P. Zucca et al. 2012). The herringbones, whose frequencies lie in the range of 30–80 MHz, last for ~ 2 minutes. The Alfvén Mach number (M_a) of the shock reaches ~ 2.4 and the kinetic energies of shock-accelerated electrons reach 2–46 keV (0.1–0.4 c), where c denotes the speed of light. Interestingly, the herringbone structures present a quasi-periodicity of 2–11 s. D. E. Morosan et al. (2019) studied the X8.2 class eruptive flare occurring in AR 12673 on 2017 September 10. The extremely fast CME at a speed of $> 3000 \text{ km s}^{-1}$ drives a shock wave ($M_a \sim 2.9$), which accelerates electrons at multiple locations along the expanding CME. Three groups of herringbones during five minutes are detected with the LOw-Frequency ARray (LOFAR; M. P. van Haarlem et al. 2013) in the frequency range 30–60 MHz. The speeds of electron beams reach up to 0.20–0.25 c .

On 2023 December 31, an X5.0 class flare occurred in NOAA AR 13536 (N04E79) close to the eastern limb. The eruptive flare was associated with a fast CME at a speed of $\sim 2852 \text{ km s}^{-1}$ recorded in the CDAW CME catalog⁷ (N. Gopalswamy et al. 2009a). Using the joint high-cadence and high-resolution observations from the Owens Valley Radio Observatory's Expanded Owens Valley Solar Array (EOVSA; D. E. Gary et al. 2018) and Long Wavelength Array (OVRO-LWA; M. M. Anderson et al. 2018), X. Chen et al. (2025) measured the magnetic field of the CME (magnetic flux rope) from low to middle corona. It is revealed that the magnetic field strength decreases rapidly from $\sim 300 \text{ G}$ at $1.02 R_{\odot}$ to $\sim 0.6 \text{ G}$ at $2.83 R_{\odot}$. Meanwhile, magnetic flux conservation of the CME is confirmed. In this paper, we focus on the quasi-periodic herringbone structures during the impulsive phase of the X-class flare, which are closely related to the distinct acceleration phase of a prominence eruption. The paper is organized as follows. Section 2 describes the instruments we use in this study. Section 3.1 shows the flare, CME, and EUV wave as a result

⁶ <https://www.e-callisto.org>

⁷ https://cdaw.gsfc.nasa.gov/CME_list/

Table 1. Properties of the instruments used in this study.

Instrument	Waveband	Cadence	Pixel Size
		(s)	(arcsec)
SDO/AIA	171, 211, 304 Å	12	0.6
LASCO-C2	WL	720	11.4
LASCO-C3	WL	720	56.0
STA/COR2	WL	900	14.7
GOES-16/SUVI	195	~60	2.5
GOES-16/SUVI	304	~120	2.5
GOES-18/XRS	0.5–4 Å, 1–8 Å	1	-
S/WAVES	0.0025–16.025 MHz	60	-
ALASKA	5–89 MHz	0.25	-
AUSTRALIA	15–87, 108–377 MHz	0.25	-
MEXICO-LANCE-B	45–90 MHz	0.25	-

of a prominence eruption. Section 3.2 shows the herringbone structures associated with the shock. Finally, a brief summary and discussions are given in Section 4.

2. INSTRUMENTS AND OBSERVATIONS

The X5.0 class flare and associated CME were observed by several telescopes, including the Atmospheric Imaging Assembly (AIA; J. R. Lemen et al. 2012) on board the Solar Dynamics Observatory (SDO; W. D. Pesnell et al. 2012), the X-Ray Sensor (XRS; F. A. Hanser & F. B. Sellers 1996) on board the Geostationary Operational Environmental Satellite 18 (GOES-18; H. A. Garcia 1994) spacecraft, the Solar Ultraviolet Imager (SUVI; S. K. Tadikonda et al. 2019; J. M. Darnel et al. 2022) on board the GOES-16 spacecraft, the C2 and C3 coronagraphs of the Large Angle Spectroscopic Coronagraph (LASCO; G. E. Brueckner et al. 1995) on board the Solar and Heliospheric Observatory (SOHO) mission, and the COR2 coronagraph of the Sun Earth Connection Coronal and Heliospheric Investigation (SECCHI; R. A. Howard et al. 2008) on board the Solar TErrestrial RElations Observatory (STEREO; M. L. Kaiser et al. 2008) ahead (hereafter STA). The separation angle between STA and the Sun-Earth connection was 6°.9 (see Fig. 2 in D. F. Ryan et al. 2024). Type III and type II radio bursts associated with the eruption are identified in the radio dynamic spectra observed by the S/WAVES (J. L. Bougeret et al. 2008) on board STA and e-Callisto AUSTRALIA. The herringbone structures were recorded by the e-Callisto AUSTRALIA, ALASKA, and MEXICO-LANCE-B. The properties of instruments and their data are summarized in Table 1.

3. RESULTS

3.1. Flare, CME, and EUV wave

In Figure 1, the top and middle panels show the eruptive prominence (EP) and X5.0 flare observed in SDO/AIA 304 and 171 Å passbands. The loop-like prominence is also evident in AIA 1600 Å images (see Fig. 2 in X. Chen et al. 2025). The EP originates from AR 13536 and rises up non-radially in the southeast direction. The inclination angle between the EP and local vertical direction is ~35°.4. The bottom panels of Figure 1 show AIA 211 Å base-difference images, featuring the EUV wave mainly propagating southward (see Fig. 2 in X. Zhang et al. 2025).

In Figure 2, the top and bottom panels show the EP, flare, and EUV wave in 304 and 195 Å base-difference images observed by GOES-16/SUVI with a larger field of view (FOV) than SDO/AIA. The EP and EUV wave have the same morphology as those in AIA images. The EUV wave starts at ~21:45:30 UT and moves on for nearly ~9 minutes (see Fig. 3 in X. Zhang et al. 2025). In panel (b2), the cyan plus symbols mark the CME leading edge observed at 21:46:19 UT when the shock and EUV wave form. The top of leading edge is estimated to have a heliocentric distance of ~1.75 R_{\odot} . To investigate the kinematics of EP and EUV wave, we select a straight slice (S1) in Figure 1(a4) and a curved slice (S2) in Figure 1(c4) with total lengths of ~303" and ~1011", respectively. Time-distance diagrams of

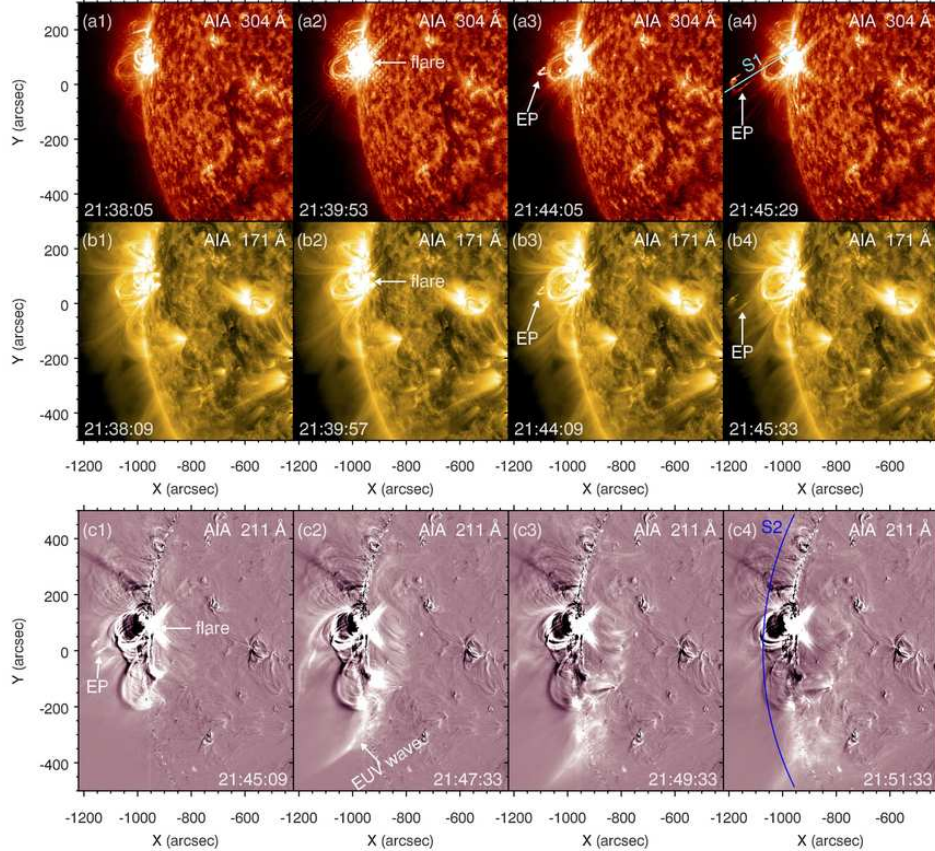


Figure 1. Top and middle panels: snapshots of AIA 304 and 171 Å images showing the non-radial prominence eruption and X5.0 flare. In panel (a4), a straight slice (S1) is used to investigate the evolution of prominence (EP). Bottom panels: snapshots of AIA 211 Å images showing the EUV wave propagating southward. In panel (c4), a curved slice (S2) is used to investigate the evolution of EUV wave.

S1 in AIA 171 and 304 Å during 21:40–21:52 UT are displayed in Figure 3(a)-(b). Trajectory of the EP along S1 is denoted with cyan plus symbols. Time-distance diagram of S2 in AIA 211 Å during 21:40–22:00 UT is displayed in Figure 3(c). The speed of EUV wave along S2 is calculated to be $\sim 600 \text{ km s}^{-1}$. To calculate the speed of EUV wave, X. Zhang et al. (2025) selected a different slice, which starts from the flare site and passes through a coronal hole. Two components of the EUV wave are derived. The faster component at a speed of $\sim 948 \text{ km s}^{-1}$ is explained by a coronal shock wave. It is noted that the two slices are situated at different altitudes. Therefore, a discrepancy in their measured velocities is reasonable (Y. Shen & Y. Liu 2012).

In Figure 4, the top and bottom panels show the halo CME and shock observed by SOHO/LASCO and STA/COR2 during 21:53–22:53 UT. The CME first appears at 21:53:30 UT and 22:00:05 UT in the FOVs of COR2 and LASCO with a central position angle of $\sim 112^\circ$. As it moves forward, a shock is driven ahead and at the CME flank, which are pointed by orange and magenta arrows. In Figure 5(b), time evolutions of the CME leading edge height in the FOVs of LASCO and COR2 are plotted with purple and magenta circles, respectively. A linear fitting (blue line) results in an apparent speed of $\sim 2839 \text{ km s}^{-1}$. Combining the observations of AIA, SUI, and LASCO, X. Chen et al. (2025) concluded that the CME leading edge also experiences a considerable acceleration. The speed increases rapidly from $\sim 1025 \text{ km s}^{-1}$ during 21:43:49–21:47:49 UT to $\sim 2807 \text{ km s}^{-1}$ during 22:00:05–22:30:05 UT. Although there is a data gap of CME observation between 21:48–21:53 UT, it is inferred that the CME leading edge experiences a continuous acceleration between 21:43 UT and 22:00 UT.

In Figure 5(a), the distances of EP along the direction of S1 in the FOVs of AIA and SUI 304 Å are drawn with yellow and orange circles, respectively. The height of EP increases rapidly from ~ 48.5 to $\sim 515.8 \text{ Mm}$ within $\sim 500 \text{ s}$. A quadratic fitting (gray dashed line) indicates a significant acceleration of $\sim 2.2 \text{ km s}^{-1}$. The speed of EP increases from ~ 393.5 to $\sim 1476.4 \text{ km s}^{-1}$. In Figure 5(b), SXR light curves of the flare during 21:30–22:10 UT in 1–8 Å

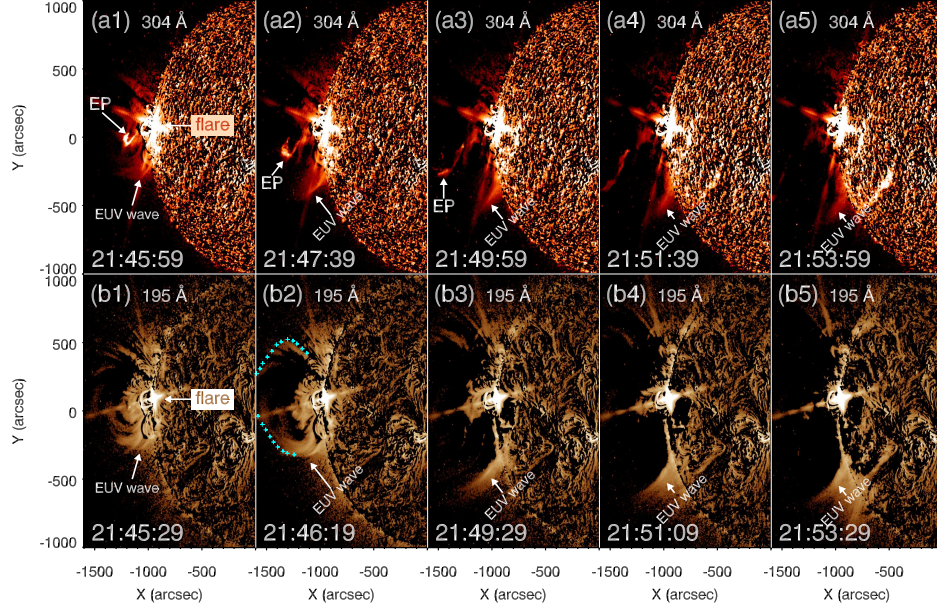


Figure 2. GOES-16/SUFI base-difference images in 304 Å (top panels) and 195 Å (bottom panels). The EP, flare, and EUV wave are labeled. In panel (b2), the cyan plus symbols denote the CME leading edge.

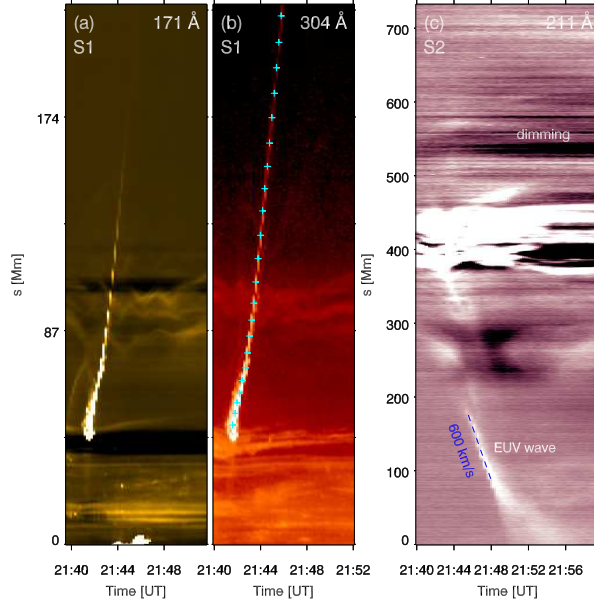


Figure 3. (a)-(b) Time-distance diagrams of S1 in AIA 171 and 304 Å. The cyan pluses signify the trajectory of the prominence along S1. (c) Time-distance diagram of S2 in AIA 211 Å. The coronal dimming and speed of EUV wave ($\sim 600 \text{ km s}^{-1}$) along S2 are labeled.

and 0.5–4 Å are drawn with maroon and green lines, respectively. The SXR fluxes start to increase at $\sim 21:36$ UT, peak at $\sim 21:55$ UT before declining gradually (see Fig. 1 in D. F. Ryan et al. 2024). Hence, the fast acceleration of the prominence occurs in the impulsive phase of the flare (X. Cheng et al. 2020). Similarly, during the non-radial propagation on 2011 February 24, the prominence experiences a remarkable acceleration ($\sim 0.98 \text{ km s}^{-2}$), which is coincident with the impulsive phase of the related flare (S. Li et al. 2025). In our case, the acceleration of prominence is ~ 2.2 times higher than that of S. Li et al. (2025).

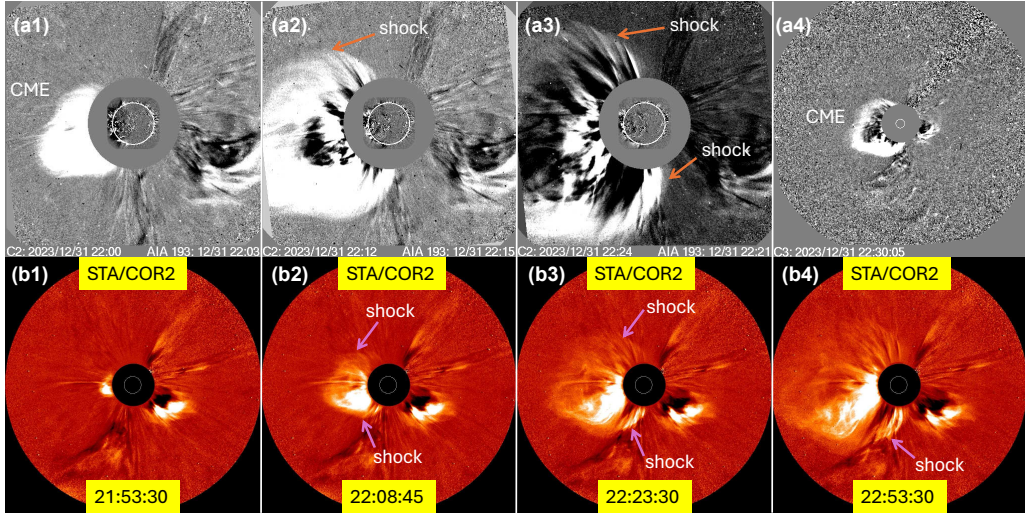


Figure 4. WL images of the halo CME and shock observed by LASCO-C2 (a1)-(a3), LASCO-C3 (a4), and STA/COR2 (b1)-(b4) during 21:53–22:53 UT.

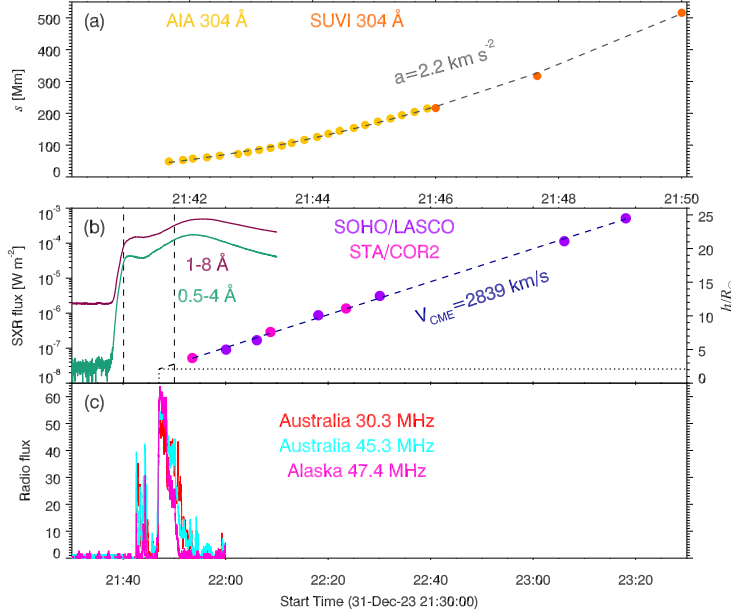


Figure 5. (a) Trajectory of the EP along S1 in the FOV of AIA (yellow circles) and SUVI (orange circles). A curve fitting (grey line) using a quadratic function results in an acceleration of $\sim 2.2 \text{ km s}^{-2}$. (b) SXR light curves of the flare in 1–8 Å (maroon line) and 0.5–4 Å (green line). Two vertical dashed lines signify the time range of panel (a). Heights of the CME leading edge in the FOVs of SOHO/LASCO and STA/COR2 are drawn with purple and magenta circles. A linear fitting (dark blue line) results in an apparent speed of $\sim 2839 \text{ km s}^{-1}$. (c) Radio fluxes of the herringbones at 30.3, 45.3, and 47.4 MHz.

Figure 6 shows radio dynamic spectra of the flare observed by e-Callisto AUSTRALIA in the frequency range 15–87 MHz (top panel) and 108–220 MHz (bottom panel) during 21:41–21:54 UT. A type III burst could be clearly identified in the frequency range 20–170 MHz during 21:42:20–21:43:00 UT. The second but much weaker type III burst occurs around 21:43:40 UT. It is generally accepted that type III bursts are produced by plasma emission of high-energy electrons escaping from the flare site along open magnetic field (M. J. Aschwanden et al. 1995; B. P. Clarke et al. 2021). Two red arrows point to the type II burst starting from $\sim 21:45:40$ UT, with the frequency drifting from ~ 160 MHz to lower values gradually. It is noticed that the beginning time of type II burst is coincident with that of EUV wave (Figure 2), indicating that the EUV wave and CME-driven shock are launched simultaneously. The subregion

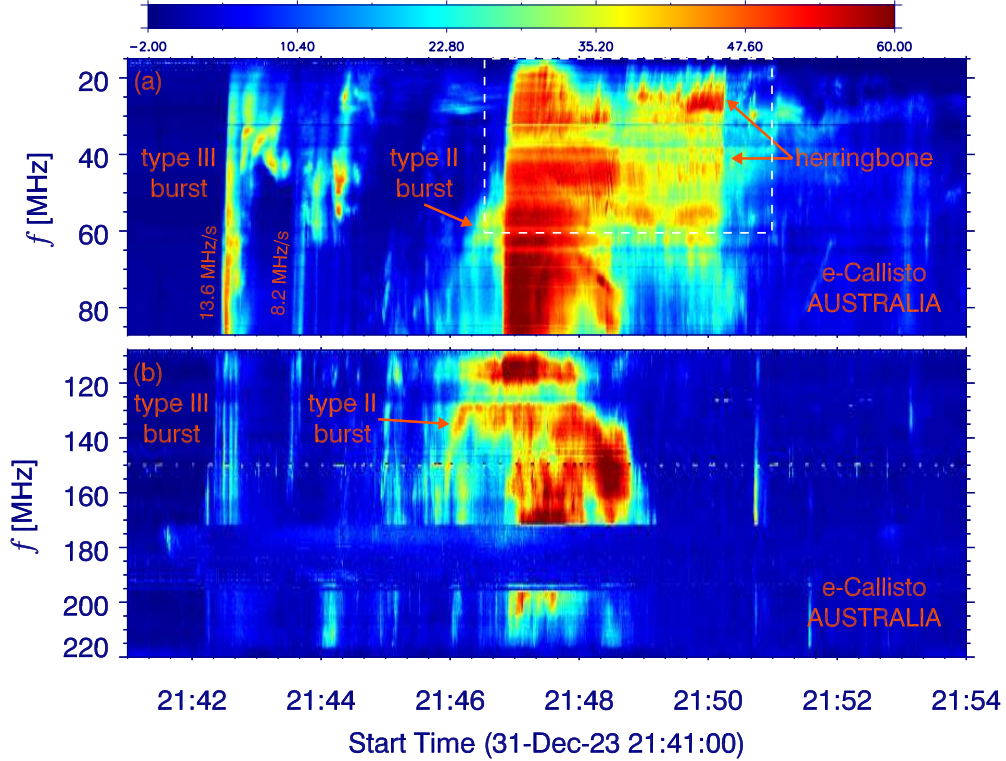


Figure 6. Radio dynamic spectra of the flare observed by e-Callisto AUSTRALIA in the frequency range 15–87 MHz (top panel) and 108–220 MHz (bottom panel). The type III bursts, type II burst, and herringbone structures are labeled. The dynamic spectra enclosed by the white dashed box are drawn in Figure 9.

within the white dashed box features herringbone structures superposed on the type II burst, which will be described in detail in the next Section.

The type III and type II bursts were also detected by S/WAVES on board STA with a lower cadence. Figure 7 shows the radio dynamic spectra of S/WAVES during 21:00–23:59 UT. Two green arrows point to the start (21:41 UT) and end (21:54 UT) moments of Figure 6. The frequency of type III bursts decreases from ~ 16 MHz to ~ 40 kHz (see Fig. 1 in [X. Chen et al. 2025](#)). The magenta arrows point to the type II burst, whose frequency decreases from ~ 16 MHz to ~ 1 MHz. Considering the time and frequency ranges, it could be correlated with the propagation of CME and associated shock in Figure 4 and considered as a natural extension of type II burst displayed in Figure 6.

3.2. Herringbone structures

As shown in Figure 6(a), there are simultaneous forward-drift and reverse-drift structures during 21:47–21:51 UT, i.e., herringbone structures ([E. P. Carley et al. 2013](#); [D. E. Morosan et al. 2019](#)). Figure 8 shows the radio dynamic spectra observed by e-Callisto ALASKA (top panel) and MEXICO-LANCE-B (bottom panel) during 21:46:30–21:51:00 UT. Due to the limitations of frequency range, only reverse-drift structures of the herringbones are detected by these telescopes, while the forward-drift structures are missing.

[E. P. Carley et al. \(2013\)](#) investigated the herringbones associated with the CME on 2011 September 22. In a follow-up work, using the image processing technique called Hough Transform ([P. V. C. Hough 1961](#)), [E. P. Carley et al. \(2015\)](#) identified 188 herringbone fine structures automatically to perform a statistical analysis. The drift rates, electron velocities, and beam displacements are derived and investigated in detail. Figure 9 shows a close-up of the dynamic spectra enclosed by the white dashed box in Figure 6(a). The time range is between 21:46:39 UT and 21:51:00 UT. The frequency range is from 15 to 60 MHz. In order to explore the herringbones in the current study, we identified 40 forward-drift and 35 reverse-drift bursts manually, which are superposed with blue dashed lines (similar to Fig. 2 in [E. P. Carley et al. 2015](#)). Parameters of these bursts could be readily obtained, including the duration (Δt), band width (BW), starting frequency (f_s), frequency drift rate ($D_f = \frac{df}{dt}$), and maximum intensity (I_{max}).

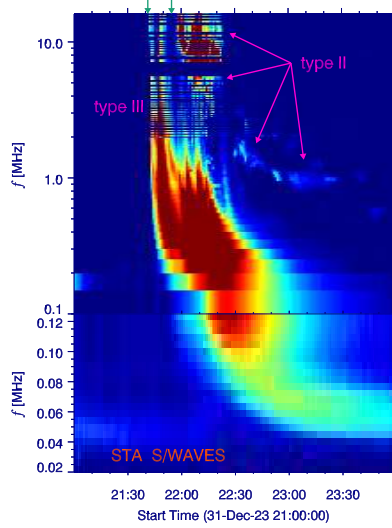


Figure 7. Radio dynamics spectra observed by S/WAVES on board STA during 21:00–23:59 UT, showing the type III and type II bursts. Two green arrows point to the start and end moments corresponding to Figure 6.

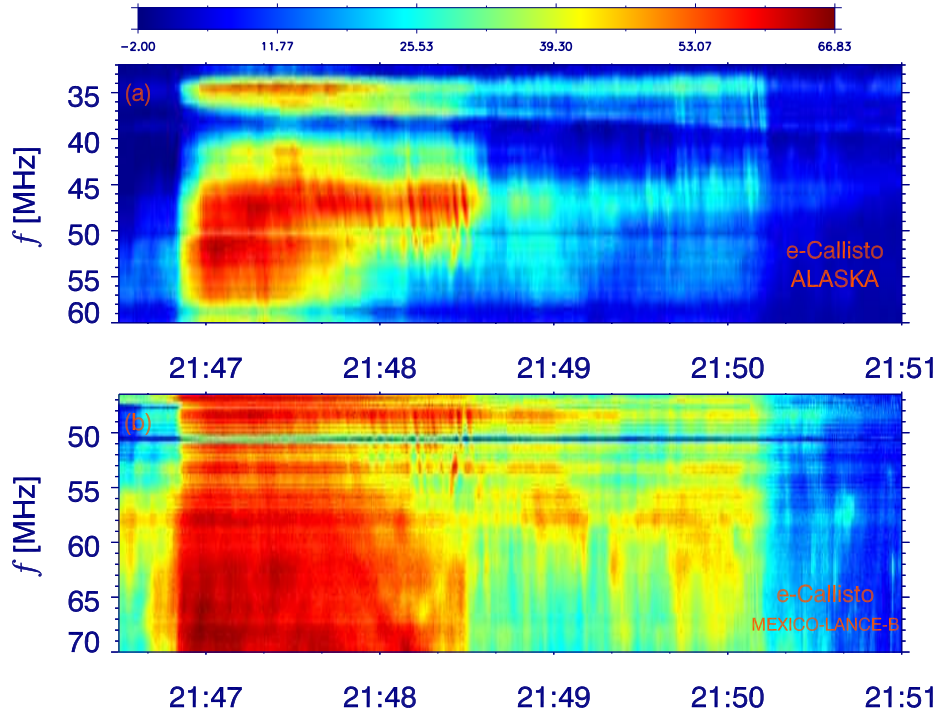


Figure 8. Radio dynamic spectra of the flare observed by e-Callisto ALASKA (a) and MEXICO-LANCE-B (b), featuring reverse-drift herringbone structures.

To estimate the velocities of electron beams (v) producing the herringbones, we use the following formula (D. E. Morosan et al. 2019):

$$v = \frac{2n_e D_f}{f} \left(\frac{dn_e}{dr} \right)^{-1}, \quad (1)$$

where $n_e(r)$ denotes the electron number density as a function of heliocentric distance (r in units of R_\odot). $\frac{dn_e}{dr}$ represents the density gradient. Here, we adopt the Newkirk electron density model (G. Newkirk 1961), which has been widely

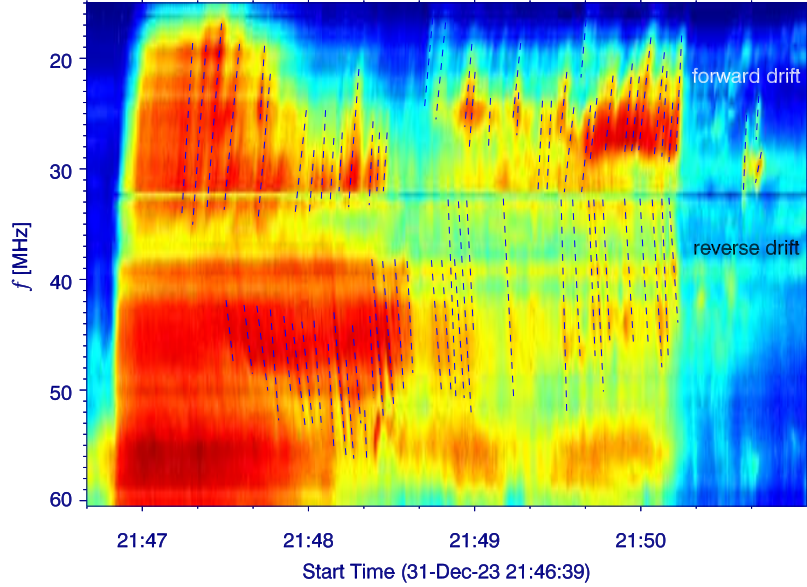


Figure 9. A close-up of the dynamic spectra during 21:46:39–21:51:00 UT. Manually identified forward-drift and reverse-drift bursts are superposed with blue dashed lines. The slopes of these bursts are used to calculate the frequency drift rates.

used:

$$n_e(r) = 4.2 \times 10^4 \times 10^{4.32/r}. \quad (2)$$

The frequency of plasma emission $f(r)$ depends solely on the electron number density $n_e(r)$:

$$f(r) = 8.98 \times \sqrt{n_e(r)}. \quad (3)$$

Figure 10 shows the histograms of these parameters for forward-drift (red color) and reverse-drift (blue color) bursts. The minimum, maximum, and mean values are listed in Table 2. In panel (a), the duration of these fine structures are between ~ 0.7 and ~ 5.6 s, with mean values of 2.5 – 3.1 s, which are very close to the statistical results of E. P. Carley et al. (2015). In panel (b), the band widths are between ~ 2.8 and ~ 20 MHz. The average band width for reverse-drift bursts is ~ 1.5 times higher than that of forward-drift ones. In panel (e), the absolute drift rates are between ~ 1.3 and ~ 9.4 MHz s $^{-1}$, with mean values of 3.6 – 4.1 MHz s $^{-1}$, which account for one third to half of the drift rates of type III bursts in Figure 6(a). V. V. Dorovskyy et al. (2015) carried out a statistical analysis on forward-drift and reverse-drift bursts of herringbone structures in the frequency range 12–30 MHz. The average values of $|\frac{df}{dt}|$ are ~ 1.23 and ~ 1.80 MHz s $^{-1}$, which account for one third to half of the values in our sample. The average values of duration are ~ 2.3 s and ~ 1.9 s, which are slightly lower than our results.

In panel (f), the corresponding electron velocities derived using Equation 1 fall in the range of 0.04 – 0.41 c . The mean value of v for forward-drift bursts is almost twice higher than that of reverse-drift bursts. On the contrary, E. P. Carley et al. (2015) found that the speed distributions of beams producing forward and reverse drift bursts show a slight difference and the total histogram peaks at ~ 0.16 c . According to Equation 1, the beam velocity is inversely proportional to the frequency and density gradient. As shown in Figure 10(d)–(e), the drift rates of forward-drift and reverse-drift bursts are comparable, while the starting frequencies have notable differences. Moreover, the density gradients of reverse-drift bursts are larger than those of forward-drift bursts. Therefore, the average velocity of beams are higher in forward-drift bursts. Additional statistical works are required to confirm the conjecture. It should be emphasized that the results of D_f and v may vary when adopting different density models (e.g., K. Saito et al. 1977; Y. Leblanc et al. 1998; G. Mann et al. 1999).

In panel (c), the maximum intensities of these bursts lie in the range of 23–54 DN. The average values of forward-drift and reverse-drift bursts are almost equal. In panel (d), the starting frequency (f_s) lies in the range of 21–52 MHz, with mean values of 30–38 MHz. According to Equation 3, the heights of shock acceleration regions are 0.64 – 0.78 R_\odot (448–546 Mm) above the photosphere, which are basically in agreement with the height of CME leading edge when the shock forms (Figure 2(b2)). In the event on 2011 September 22, the separatrix frequency between the forward-drift

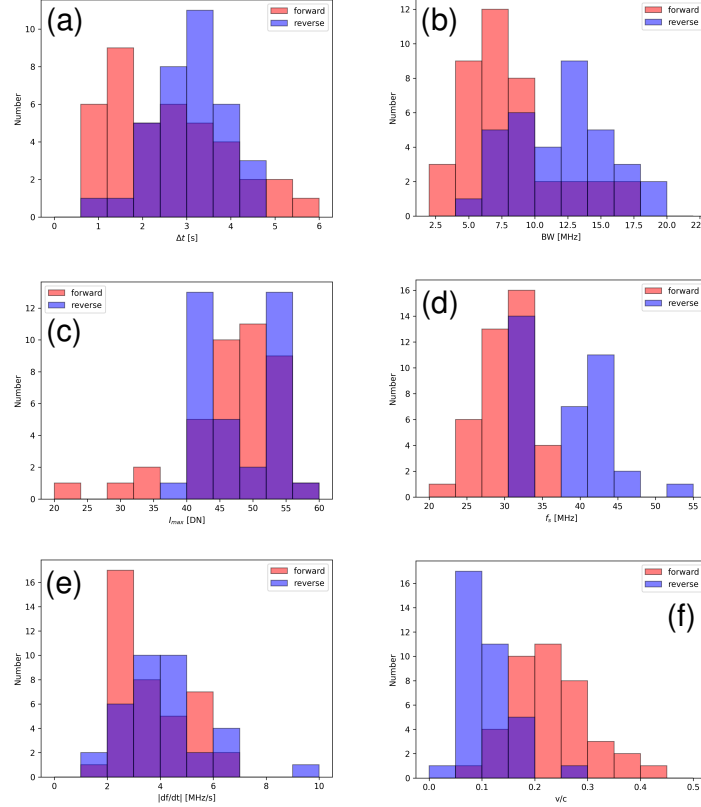


Figure 10. Histograms of the parameters for forward-drift (red color) and reverse-drift (blue color) herringbone bursts, including the duration (a), band width (b), maximum intensity (c), starting frequency (d), frequency drift rate (e), and electron beam velocity (f).

and reverse-drift structures drifts from ~ 43 to ~ 32 MHz (E. P. Carley et al. 2015). The corresponding height of shock acceleration increases from ~ 0.57 to $\sim 0.74 R_\odot$ using the Newkirk model. In the event on 2017 September 10, the separatrix frequency is around 40 MHz. It is noted that the fine structures of herringbone in our study are selected by eye rather than automatically. Consequently, the derived parameters of these bursts may have some uncertainties. Nevertheless, comparisons with previous works indicate that the average values are generally in accordance with their findings.

The radio dynamic spectra of AUSTRALIA, ALASKA, and MEXICO-LANCE-B (Figures 8 and 9) show that the bursts of herringbone structures appear intermittently, suggesting that electrons are accelerated quasi-periodically (E. P. Carley et al. 2013). To explore the periods of herringbones, we extract the radio fluxes at 30.3 and 45.3 MHz from AUSTRALIA observations and 47.4 MHz from ALASKA observations. Time evolutions of these fluxes are plotted in Figure 5(c). The slowly-varying components of the fluxes are derived using the smoothing method with a window of ~ 30 s. The fast-varying components are background-removed fluxes. The wavelet transforms of the fast-varying components are displayed in Figure 11. It is clear that the radio fluxes have QPPs with periods of ~ 17.5 , ~ 21.0 , and ~ 21.3 s at 30.3, 45.3, and 47.4 MHz. These periods are longer than those reported by E. P. Carley et al. (2013).

4. SUMMARY AND DISCUSSIONS

In this paper, we report quasi-periodic herringbone structures during the impulsive phase of an X5.0 flare, coinciding with the distinct acceleration phase of eruptive prominence ejection. The flare results from the prominence eruption in NOAA AR 13536 on 2023 December 31. The prominence propagates non-radially in the southeast direction with an inclination angle of $\sim 35^\circ$. The speed of prominence increases from ~ 394 to ~ 1476 km s $^{-1}$ within ~ 500 s. The fast CME at a speed of ~ 2852 km s $^{-1}$ drives a shock wave and a coronal EUV wave observed in WL coronagraphs and EUV images, respectively. The herringbone structures lasting for ~ 4 minutes take place at the initial stage of a group of type II burst. The herringbones in the frequency range 20–70 MHz are characterized by simultaneous

Table 2. Statistic analysis of forward-drift and reverse-drift herringbone structures, including the duration (Δt), band width (BW), frequency drift rate ($\frac{df}{dt}$), starting frequency (f_s), maximal intensity (I_{max}), and electron velocity (v).

Type	Value	Δt	BW	$ \frac{df}{dt} $	f_s	I_{max}	v
		(s)	(MHz)	(MHz s^{-1})	(MHz)	(DN)	(c)
Forward-drift	Min.	0.69	2.78	1.33	21.74	23.58	0.07
Forward-drift	Max.	5.56	16.94	6.39	35.05	56.83	0.41
Forward-drift	Mean	2.54	8.12	3.61	30.18	47.38	0.23
Reverse-drift	Min.	0.69	4.29	1.95	32.61	38.40	0.04
Reverse-drift	Max.	4.64	19.64	9.44	51.82	56.36	0.26
Reverse-drift	Mean	3.07	11.91	4.13	38.45	48.15	0.11

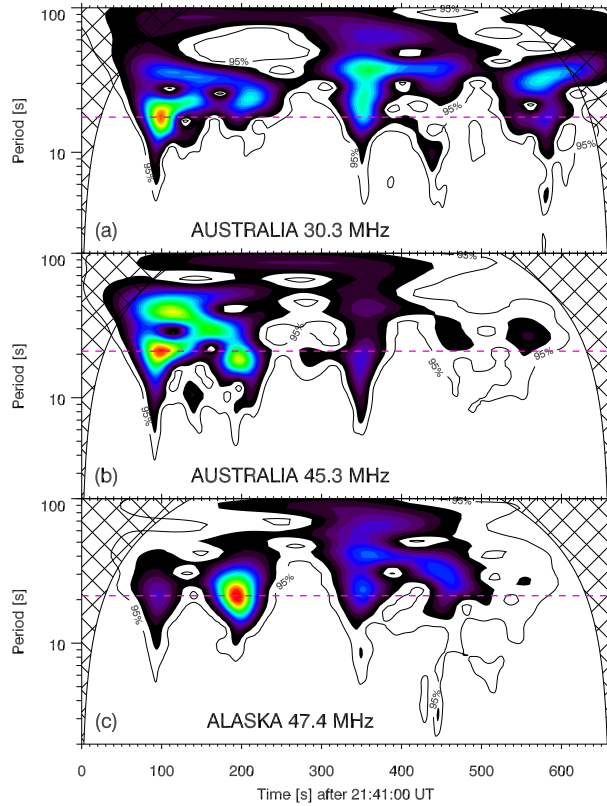


Figure 11. Wavelet transforms of the radio fluxes at 30.3 (a), 45.3 (b), and 47.4 MHz (c). The magenta dashed lines represent the corresponding periods.

forward-drift and reverse-drift stripes with average durations of ~ 2.5 s and ~ 3.1 s. The frequency drift rates of these bursts range from ~ 1.3 to ~ 9.4 MHz s^{-1} with average values of ~ 3.6 and ~ 4.1 MHz s^{-1} , respectively. The heights of particle acceleration regions are estimated to be 0.64 – $0.78 R_{\odot}$ (448–546 Mm) above the photosphere. The speeds of electron beams producing the herringbones are estimated to be 0.04 – $0.41 c$, with average values of $\sim 0.23 c$ and $\sim 0.11 c$ for forward-drift and reverse-drift bursts. QPPs with periods of 17.5 – 21.3 s are discovered in the radio fluxes of herringbones, indicating quasi-periodic accelerations of electrons by the shock wave.

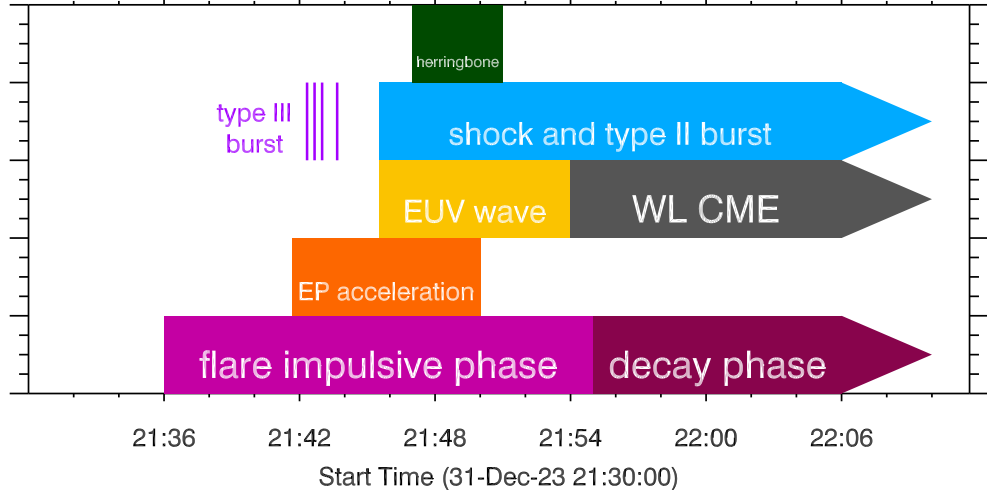


Figure 12. Time line of the activities during the eruptive flare on 2023 December 31.

Although shock waves and type II radio bursts associated with CMEs are frequently observed (B. Vršnak et al. 2006; N. Gopalswamy et al. 2013, 2019; Q. Zhang et al. 2022; W. W. Pan et al. 2025), herringbone structures are rarely detected (I. H. Cairns & R. D. Robinson 1987; J. Magdalenić et al. 2020; E. P. Carley et al. 2021; D. E. Morosan et al. 2022, 2024). In the era of SDO since 2010, there are several eruptive flares showing unambiguous herringbone structures in the radio dynamic spectra (e.g., E. P. Carley et al. 2013; D. E. Morosan et al. 2019). In Table 3, the parameters of these events and the event in this study are summarized, including the date, location, flare class, CME speed (v_{CME}), EUV wave speed (v_{wave}), Alfvén Mach number (M_a) of the shock, duration (τ_{HB}) and frequency range of herringbone (f_{HB}), and electron beam speed (v). All these events are related to shocks with large M_a . It seems that herringbones are closely related to large eruptive flares, accompanied by strong shock waves, especially quasi-perpendicular shocks, which are capable of accelerating electrons to high energies efficiently (G. D. Holman & M. E. Pesses 1983; J. Giacalone 2005; G. P. Zank et al. 2006; E. P. Carley et al. 2021; G. Mann et al. 2022). To investigate how solar energetic particle events are created by coronal shocks, X. Kong et al. (2017) studied the process in which a fast shock propagates through a streamer-like magnetic field including both closed and open field lines. Particles are efficiently accelerated due to perpendicular shock geometry. D. E. Morosan et al. (2022) investigated the herringbones associated with a coronal EUV wave generated by fast CME expansion on 2013 October 25. It is concluded that the CME and related shock wave propagate quasi-perpendicularly to the streamer where herringbones are created. The interaction between the CME shock and streamer is favorable to the production of electron beams that generate herringbones due to shock drift acceleration. A. Koval et al. (2023) analyzed the type II burst associated with the CME/shock on 2014 July 25. The herringbone type II was generated when the CME/shock penetrated into the lower part of the streamer below its cusp point.

Figure 12 shows a time line of the activities during the X5.0-class eruptive flare. It is clear that the prominence acceleration occurs during the impulsive phase of the flare, giving rise to the formation of CME leading edge seen in EUV wavelengths. The EUV wave and shock wave associated with the type II burst start at $\sim 21:45:30$ UT. The herringbone structures superposed on the type II burst are evident during 21:47–21:51 UT. According to the schematic cartoons showing the locations of herringbone sources from different perspectives (see Fig. 3 in D. E. Morosan et al. 2019), the forward-drift and reverse-drift stripes are due to electron beams moving outward and toward the sun along open field. Therefore, the high-energy electrons are released and herringbones are generated once the shock wave encounters open field during its expansion. In the future, statistical analysis is worthwhile to figure out the physical origin and properties of herringbone structures in depth. Numerical simulations are required to investigate particle accelerations by coronal shock waves.

Table 3. Comparison of the events producing herringbone structures.

Date	AR	Flare	v_{CME}	v_{wave}	M_a	τ_{HB}	f_{HB}	v	Reference
			(km s $^{-1}$)	(km s $^{-1}$)		(min)	(MHz)	(c)	
2011/06/07	11226	M2.0	1950	-	-	~20	12–30	-	V. V. Dorovskyy et al. (2015)
2011/09/22	11302	X1.4	1905	480	2.4	~2	10–90	0.1–0.4	E. P. Carley et al. (2013)
2013/10/25	11882	X2.1	1081	-	~5	~2	150–260	-	D. E. Morosan et al. (2022)
2014/08/25	12146	M2.0	555	-	-	~2	62–82	-	J. Magdalenić et al. (2020)
2017/09/10	12673	X8.2	3038	850	2.9	~5	30–60	0.2–0.25	D. E. Morosan et al. (2019)
2019/03/20	12736	C4.8	500	950	-	~4	30–50	0.19	E. P. Carley et al. (2021)
2022/03/28	12975	M4.0	702	600	~8	>10	25–250	0.18	D. E. Morosan et al. (2024)
2023/12/31	13536	X5.0	2852	600	-	~4	20–70	0.04–0.41	this work

ACKNOWLEDGMENTS

The authors appreciate the reviewer for his/her valuable suggestions and comments to improve the quality of this article. We also thank Dr. Jun Dai, Profs. Yao Chen and Yihua Yan for discussions. SDO is a mission of NASA's Living With a Star Program. AIA data are courtesy of the NASA/SDO science teams. STEREO/SECCHI data are provided by a consortium of US, UK, Germany, Belgium, and France. The e-Callisto data are courtesy of the Institute for Data Science FHNW Brugg/Windisch, Switzerland. This CME catalog is generated and maintained at the CDAW Data Center by NASA and The Catholic University of America in cooperation with the Naval Research Laboratory. SOHO is a project of international cooperation between ESA and NASA. This work is supported by the National Key R&D Program of China 2021YFA1600500 (2021YFA1600502), 2022YFF0503002 (2022YFF0503000), the Strategic Priority Research Program of the Chinese Academy of Sciences, grant No. XDB0560000, NSFC under the grant numbers 12373065, 12333010, 12325303, 12403068, Natural Science Foundation of Jiangsu Province (BK20231510 and BK20241707), and the Yunnan Key Laboratory of Solar Physics and Space Science, under the number 202205AG070009.

REFERENCES

Anderson, M. M., Hallinan, G., Eastwood, M. W., et al. 2018, ApJ, 864, 22, doi: [10.3847/1538-4357/aad2d7](https://doi.org/10.3847/1538-4357/aad2d7)

Aschwanden, M. J., Benz, A. O., Dennis, B. R., & Schwartz, R. A. 1995, ApJ, 455, 347, doi: [10.1086/176582](https://doi.org/10.1086/176582)

Aurass, H., Vršnak, B., & Mann, G. 2002, A&A, 384, 273, doi: [10.1051/0004-6361:20011735](https://doi.org/10.1051/0004-6361:20011735)

Bale, S. D., Reiner, M. J., Bougeret, J. L., et al. 1999, Geophys. Res. Lett., 26, 1573, doi: [10.1029/1999GL900293](https://doi.org/10.1029/1999GL900293)

Ball, L., & Melrose, D. B. 2001, PASA, 18, 361, doi: [10.1071/AS01047](https://doi.org/10.1071/AS01047)

Benz, A. O., Monstein, C., Meyer, H., et al. 2009, Earth Moon and Planets, 104, 277, doi: [10.1007/s11038-008-9267-6](https://doi.org/10.1007/s11038-008-9267-6)

Bougeret, J. L., Goetz, K., Kaiser, M. L., et al. 2008, SSRv, 136, 487, doi: [10.1007/s11214-007-9298-8](https://doi.org/10.1007/s11214-007-9298-8)

Brueckner, G. E., Howard, R. A., Koomen, M. J., et al. 1995, SoPh, 162, 357, doi: [10.1007/BF00733434](https://doi.org/10.1007/BF00733434)

Burgess, D. 2006, ApJ, 653, 316, doi: [10.1086/508805](https://doi.org/10.1086/508805)

Cairns, I. H., & Robinson, R. D. 1987, SoPh, 111, 365, doi: [10.1007/BF00148526](https://doi.org/10.1007/BF00148526)

Cane, H. V., & White, S. M. 1989, SoPh, 120, 137, doi: [10.1007/BF00148539](https://doi.org/10.1007/BF00148539)

Carley, E. P., Long, D. M., Byrne, J. P., et al. 2013, Nature Physics, 9, 811, doi: [10.1038/nphys2767](https://doi.org/10.1038/nphys2767)

Carley, E. P., Reid, H., Vilmer, N., & Gallagher, P. T. 2015, A&A, 581, A100, doi: [10.1051/0004-6361/201526251](https://doi.org/10.1051/0004-6361/201526251)

Carley, E. P., Cecconi, B., Reid, H. A., et al. 2021, ApJ, 921, 3, doi: [10.3847/1538-4357/ac1acd](https://doi.org/10.3847/1538-4357/ac1acd)

Chen, B., Bastian, T. S., Shen, C., et al. 2015, Science, 350, 1238, doi: [10.1126/science.aac8467](https://doi.org/10.1126/science.aac8467)

Chen, X., Yan, Y., Tan, B., et al. 2019, ApJ, 878, 78, doi: [10.3847/1538-4357/ab1d64](https://doi.org/10.3847/1538-4357/ab1d64)

Chen, X., Chen, B., Yu, S., et al. 2025, *ApJL*, 990, L50, doi: [10.3847/2041-8213/adfa71](https://doi.org/10.3847/2041-8213/adfa71)

Cheng, X., Zhang, J., Kliem, B., et al. 2020, *ApJ*, 894, 85, doi: [10.3847/1538-4357/ab886a](https://doi.org/10.3847/1538-4357/ab886a)

Clarke, B. P., Hayes, L. A., Gallagher, P. T., Maloney, S. A., & Carley, E. P. 2021, *ApJ*, 910, 123, doi: [10.3847/1538-4357/abe463](https://doi.org/10.3847/1538-4357/abe463)

Darnel, J. M., Seaton, D. B., Bethge, C., et al. 2022, *Space Weather*, 20, e2022SW003044, doi: [10.1029/2022SW00304410.1002/essoar.10510311.1](https://doi.org/10.1029/2022SW00304410.1002/essoar.10510311.1)

Dorovskyy, V. V., Melnik, V. N., Konovalenko, A. A., et al. 2015, *SoPh*, 290, 2031, doi: [10.1007/s11207-015-0725-9](https://doi.org/10.1007/s11207-015-0725-9)

Dulk, G. A. 1985, *ARA&A*, 23, 169, doi: [10.1146/annurev.aa.23.090185.001125](https://doi.org/10.1146/annurev.aa.23.090185.001125)

Fletcher, L., Dennis, B. R., Hudson, H. S., et al. 2011, *SSRv*, 159, 19, doi: [10.1007/s11214-010-9701-8](https://doi.org/10.1007/s11214-010-9701-8)

Garcia, H. A. 1994, *SoPh*, 154, 275, doi: [10.1007/BF00681100](https://doi.org/10.1007/BF00681100)

Gary, D. E., Chen, B., Dennis, B. R., et al. 2018, *ApJ*, 863, 83, doi: [10.3847/1538-4357/aad0ef](https://doi.org/10.3847/1538-4357/aad0ef)

Giacalone, J. 2005, *ApJ*, 624, 765, doi: [10.1086/429265](https://doi.org/10.1086/429265)

Gopalswamy, N., Mäkelä, P., & Yashiro, S. 2019, *Sun and Geosphere*, 14, 111, doi: [10.31401/SunGeo.2019.02.03](https://doi.org/10.31401/SunGeo.2019.02.03)

Gopalswamy, N., Yashiro, S., Michalek, G., et al. 2009a, *Earth Moon and Planets*, 104, 295, doi: [10.1007/s11038-008-9282-7](https://doi.org/10.1007/s11038-008-9282-7)

Gopalswamy, N., Thompson, W. T., Davila, J. M., et al. 2009b, *SoPh*, 259, 227, doi: [10.1007/s11207-009-9382-1](https://doi.org/10.1007/s11207-009-9382-1)

Gopalswamy, N., Xie, H., Mäkelä, P., et al. 2013, *Advances in Space Research*, 51, 1981, doi: [10.1016/j.asr.2013.01.006](https://doi.org/10.1016/j.asr.2013.01.006)

Guo, F., & Giacalone, J. 2010, *ApJ*, 715, 406, doi: [10.1088/0004-637X/715/1/406](https://doi.org/10.1088/0004-637X/715/1/406)

Hanser, F. A., & Sellers, F. B. 1996, in *Society of Photo-Optical Instrumentation Engineers (SPIE) Conference Series*, Vol. 2812, GOES-8 and Beyond, ed. E. R. Washwell, 344–352, doi: [10.1117/12.254082](https://doi.org/10.1117/12.254082)

Holman, G. D., & Pesses, M. E. 1983, *ApJ*, 267, 837, doi: [10.1086/160918](https://doi.org/10.1086/160918)

Hough, P. V. C. 1961, in *Instrumentation for High-Energy Physics*, 242

Howard, R. A., Moses, J. D., Vourlidas, A., et al. 2008, *SSRv*, 136, 67, doi: [10.1007/s11214-008-9341-4](https://doi.org/10.1007/s11214-008-9341-4)

Inglis, A. R., Nakariakov, V. M., & Melnikov, V. F. 2008, *A&A*, 487, 1147, doi: [10.1051/0004-6361:20079323](https://doi.org/10.1051/0004-6361:20079323)

Kaiser, M. L., Kucera, T. A., Davila, J. M., et al. 2008, *SSRv*, 136, 5, doi: [10.1007/s11214-007-9277-0](https://doi.org/10.1007/s11214-007-9277-0)

Kong, X., Guo, F., Giacalone, J., Li, H., & Chen, Y. 2017, *ApJ*, 851, 38, doi: [10.3847/1538-4357/aa97d7](https://doi.org/10.3847/1538-4357/aa97d7)

Koval, A., Stanislavsky, A., Karlický, M., et al. 2023, *ApJ*, 952, 51, doi: [10.3847/1538-4357/acdbcc](https://doi.org/10.3847/1538-4357/acdbcc)

Leblanc, Y., Dulk, G. A., & Bougeret, J.-L. 1998, *SoPh*, 183, 165, doi: [10.1023/A:1005049730506](https://doi.org/10.1023/A:1005049730506)

Lemen, J. R., Title, A. M., Akin, D. J., et al. 2012, *SoPh*, 275, 17, doi: [10.1007/s11207-011-9776-8](https://doi.org/10.1007/s11207-011-9776-8)

Li, S., Zhang, Q., Ji, H., et al. 2025, *ApJ*, 993, 99, doi: [10.3847/1538-4357/ae0a53](https://doi.org/10.3847/1538-4357/ae0a53)

Magdalenić, J., Marqué, C., Fallows, R. A., et al. 2020, *ApJL*, 897, L15, doi: [10.3847/2041-8213/ab9abc](https://doi.org/10.3847/2041-8213/ab9abc)

Mann, G., Aurass, H., Voigt, W., & Paschke, J. 1992, in *ESA Special Publication*, Vol. 348, *Coronal Streamers, Coronal Loops, and Coronal and Solar Wind Composition*, ed. C. Mattok, 129–132

Mann, G., & Classen, H. T. 1995, *A&A*, 304, 576

Mann, G., Classen, T., & Aurass, H. 1995, *A&A*, 295, 775

Mann, G., Jansen, F., MacDowall, R. J., Kaiser, M. L., & Stone, R. G. 1999, *A&A*, 348, 614

Mann, G., & Klassen, A. 2002, in *ESA Special Publication*, Vol. 1, *Solar Variability: From Core to Outer Frontiers*, ed. A. Wilson, 245–248

Mann, G., & Klassen, A. 2005, *A&A*, 441, 319, doi: [10.1051/0004-6361:20034396](https://doi.org/10.1051/0004-6361:20034396)

Mann, G., Vocks, C., Warmuth, A., et al. 2022, *A&A*, 660, A71, doi: [10.1051/0004-6361/202142201](https://doi.org/10.1051/0004-6361/202142201)

Miteva, R., & Mann, G. 2007, *A&A*, 474, 617, doi: [10.1051/0004-6361:20066856](https://doi.org/10.1051/0004-6361:20066856)

Morosan, D. E., Pomoell, J., Kumari, A., Vainio, R., & Kilpua, E. K. J. 2022, *A&A*, 668, A15, doi: [10.1051/0004-6361/202244432](https://doi.org/10.1051/0004-6361/202244432)

Morosan, D. E., Carley, E. P., Hayes, L. A., et al. 2019, *Nature Astronomy*, 3, 452, doi: [10.1038/s41550-019-0689-z](https://doi.org/10.1038/s41550-019-0689-z)

Morosan, D. E., Pomoell, J., Palmroos, C., et al. 2024, *A&A*, 683, A31, doi: [10.1051/0004-6361/202347873](https://doi.org/10.1051/0004-6361/202347873)

Newkirk, Jr., G. 1961, *ApJ*, 133, 983, doi: [10.1086/147104](https://doi.org/10.1086/147104)

Pan, W. W., Zhang, Q. M., & Qiu, Y. 2025, *MNRAS*, 542, 1308, doi: [10.1093/mnras/staf1188](https://doi.org/10.1093/mnras/staf1188)

Pesnell, W. D., Thompson, B. J., & Chamberlin, P. C. 2012, *SoPh*, 275, 3, doi: [10.1007/s11207-011-9841-3](https://doi.org/10.1007/s11207-011-9841-3)

Roberts, J. A. 1959, *Australian Journal of Physics*, 12, 327, doi: [10.1071/PH590327](https://doi.org/10.1071/PH590327)

Ryan, D. F., Massa, P., Battaglia, A. F., et al. 2024, *SoPh*, 299, 114, doi: [10.1007/s11207-024-02341-8](https://doi.org/10.1007/s11207-024-02341-8)

Saito, K., Poland, A. I., & Munro, R. H. 1977, *SoPh*, 55, 121, doi: [10.1007/BF00150879](https://doi.org/10.1007/BF00150879)

Shen, Y., & Liu, Y. 2012, *ApJL*, 752, L23, doi: [10.1088/2041-8205/752/2/L23](https://doi.org/10.1088/2041-8205/752/2/L23)

Tadikonda, S. K., Freesland, D. C., Minor, R. R., et al. 2019, *SoPh*, 294, 28, doi: [10.1007/s11207-019-1411-0](https://doi.org/10.1007/s11207-019-1411-0)

van Haarlem, M. P., Wise, M. W., Gunst, A. W., et al. 2013, *A&A*, 556, A2, doi: [10.1051/0004-6361/201220873](https://doi.org/10.1051/0004-6361/201220873)

Vandas, M., & Karlický, M. 2011, *A&A*, 531, A55, doi: [10.1051/0004-6361/201016135](https://doi.org/10.1051/0004-6361/201016135)

Vršnak, B., Magdalenić, J., Aurass, H., & Mann, G. 2002, *A&A*, 396, 673, doi: [10.1051/0004-6361:20021413](https://doi.org/10.1051/0004-6361:20021413)

Vršnak, B., Warmuth, A., Temmer, M., et al. 2006, *A&A*, 448, 739, doi: [10.1051/0004-6361:20053740](https://doi.org/10.1051/0004-6361:20053740)

Zank, G. P., Li, G., Florinski, V., et al. 2006, *Journal of Geophysical Research (Space Physics)*, 111, A06108, doi: [10.1029/2005JA011524](https://doi.org/10.1029/2005JA011524)

Zank, G. P., Li, G., & Verkhoglyadova, O. 2007, *SSRv*, 130, 255, doi: [10.1007/s11214-007-9214-2](https://doi.org/10.1007/s11214-007-9214-2)

Zhang, Q., Li, C., Li, D., et al. 2022, *ApJL*, 937, L21, doi: [10.3847/2041-8213/ac8e01](https://doi.org/10.3847/2041-8213/ac8e01)

Zhang, Q., Teng, W., Li, D., Dai, J., & Zhang, Y. 2023, *ApJ*, 958, 85, doi: [10.3847/1538-4357/ad05bc](https://doi.org/10.3847/1538-4357/ad05bc)

Zhang, Q. M., Li, D., & Ning, Z. J. 2016, *ApJ*, 832, 65, doi: [10.3847/0004-637X/832/1/65](https://doi.org/10.3847/0004-637X/832/1/65)

Zhang, X., Chen, H., Zhou, G., et al. 2025, *ApJL*, 987, L3, doi: [10.3847/2041-8213/ade38c](https://doi.org/10.3847/2041-8213/ade38c)

Zimovets, I. V., McLaughlin, J. A., Srivastava, A. K., et al. 2021, *SSRv*, 217, 66, doi: [10.1007/s11214-021-00840-9](https://doi.org/10.1007/s11214-021-00840-9)

Zlobec, P., Messerotti, M., Karlický, M., & Urbarz, H. 1993, *SoPh*, 144, 373, doi: [10.1007/BF00627601](https://doi.org/10.1007/BF00627601)

Zucca, P., Carley, E. P., Bloomfield, D. S., & Gallagher, P. T. 2014, *A&A*, 564, A47, doi: [10.1051/0004-6361/201322650](https://doi.org/10.1051/0004-6361/201322650)

Zucca, P., Carley, E. P., McCauley, J., et al. 2012, *SoPh*, 280, 591, doi: [10.1007/s11207-012-9992-x](https://doi.org/10.1007/s11207-012-9992-x)